8806 *Biochemistry* **2009,** *48,* 8806–8816
DOI: 10.1021/bi9007462

BIOCHEMISTRY
including biophysical chemistry & molecular biology
*Article*

# Arsenic Metalation of Seaweed *Fucus vesiculosus* Metallothionein: The Importance of the Interdomain Linker in Metallothionein[†]

Thanh T. Ngu, Janice A. Lee, Moira K. Rushton, and Martin J. Stillman*

*Department of Chemistry, University of Western Ontario, London, Ontario, Canada N6A 5B7*

*Received April 30, 2009; Revised Manuscript Received August 4, 2009*

ABSTRACT: The presence of metallothionein in seaweed *Fucus vesiculosus* has been suggested as the protecting agent against toxic metals in the contaminated waters it can grow in. We report the first kinetic pathway data for $As^{3+}$ binding to an algal metallothionein, *F. vesiculosus* metallothionein (rfMT). The time and temperature dependence of the relative concentrations of apo-rfMT and the five As-containing species have been determined following mixing of $As^{3+}$ and apo-rfMT using electrospray ionization mass spectrometry (ESI MS). Kinetic analysis of the detailed time-resolved mass spectral data for $As^{3+}$ metalation allows the simulation of the metalation reactions showing the consumption of apo-rfMT, the formation and consumption of $As_1$- to $As_4$-rfMT, and subsequent, final formation of $As_5$-rfMT. The kinetic model proposed here provides a stepwise analysis of the metalation reaction showing time-resolved occupancy of the $Cys_7$ and the $Cys_9$ domain. The rate constants ($M^{-1}$ $s^{-1}$) calculated from the fits for the 7-cysteine $\gamma$ domain are $k_{1\gamma}$, 19.8, and $k_{2\gamma}$, 1.4, and for the 9-cysteine $\beta$ domain are $k_{1\beta}$, 16.3, $k_{2\beta}$, 9.1, and $k_{3\beta}$, 2.2. The activation energies and Arrhenius factors for each of the reaction steps are also reported. rfMT has a long 14 residue linker, which as we show from analysis of the ESI MS data, allows each of its two domains to bind $As^{3+}$ independently of each other. The analysis provides for the first time an explanation of the differing metal-binding properties of two-domain MTs with linkers of varying lengths, suggesting further comparison between plant (with long linkers) and mammalian (with short linkers) metallothioneins will shed light on the role of the interdomain linker.

The brown seaweed *Fucus vesiculosus* grows in and is resistant to toxic metals in polluted waters and, as such, is a potential biomarker for toxic metal levels in aquatic environments. Arsenic contaminated water is a worldwide threat to humans and is reported to currently affect millions of people (*1*, *2*). When ingested, As is believed to bind to biological sulfur side chains in amino acids. Metallothioneins are rich in sulfur with up to 30% of the amino acids being cysteine, and the gene for metallothionein in *F. vesiculosus* has been reported (*3*). Recombinant metallothionein from *F. vesiculosus* (rfMT)[1] has been reported to remediate arsenic (*4*). rfMT binds 6 $Cd^{2+}$ (*5*) or 5 $As^{3+}$ ions (*6*) to the thiols of the 16 cysteines in the sequence.

The metalloprotein metallothionein discovered in 1957 (*7*) is ubiquitous across all organisms; it has been characterized from mammals, plants, invertebrates, yeast, and many other species (*8*, *9*). Metallothioneins exhibit remarkable metal-binding properties for a very wide range of metals (*8*, *9*). Metal coordination takes place through the large number of cysteine sulfurs present in the protein forming two metal-binding domains in mammalian, crustacean, plant, and algal MTs (*3*, *8*−*10*). Each of the monovalent group 11 and the divalent group 12 metals binds to the protein, and based on X-ray diffraction, NMR, XANES, and XAFS studies it is proposed that all of these metals bind in metal−thiolate clusters in the two domains (*11*, *12*). It has been shown that seven divalent metals and up to 12 Cu(I) and Ag(I) bind to the mammalian in a 9-cysteine $\beta$ and an 11-cysteine $\alpha$ domain, where the domains are connected by a short linker region (*8*, *9*). On the other hand, plant MTs (types 1−3) generally consist of two cysteine-rich regions separated by a long interdomain linker that is approximately 40 amino acids in length (*10*, *13*, *14*). The structures for these plant MTs have been proposed to consist of either a hairpin motif (*15*) or two separate metal−thiolate clusters (*16*, *17*).

rfMT has a 67 amino acid sequence within which are two regions high in cysteines: a seven-cysteine region (named $\gamma$) and a nine-cysteine region (named $\beta$). These two regions are separated by a 14 amino acid linker. Strikingly, rfMT has a much longer linker than mammalian MT (only 2−3 amino acids long in native proteins), which is expected to give rfMT a much more flexible structure (*18*). Similar to mammalian MT, it has been proposed from studies of $Cd^{2+}$ binding to rfMT that the metals bind in two domains: 3 $Cd^{2+}$ to the 7-cysteine $\gamma$ and 3 $Cd^{2+}$ to the 9-cysteine $\beta$ domain (*5*, *6*). A 7-cysteine $\gamma$ domain has not been reported for other metallothioneins.

Despite the extensive reports of metalation reactions with a wide range of metals (*19*−*24*), the experimental evidence for the mechanism for the metalation reaction in metallothioneins has remained elusive until recently. This is mainly because the

[†]We thank NSERC of Canada for financial support through operating funds (to M.J.S.) and Canada Graduate Scholarship (CGS) (to T.T. N.).

*To whom correspondence should be addressed. E-mail: Martin.Stillman@uwo.ca. Tel: 1-519-661-3821. Fax: 1-519-661-3022.

[1]Abbreviations: αhMT, α domain of human metallothionein 1a; apo-MT, metal-free metallothionein; βαhMT, two-domain βα human metallothionein 1a; βhMT, β domain of human metallothionein 1a; βrfMT, β domain of recombinant *Fucus vesiculosus* metallothionein; ESI, electrospray ionization; EXAFS, extended X-ray absorption fine structure; γrfMT, γ domain of recombinant *F. vesiculosus* metallothionein; holo-MT, fully metalated or native metallothionein; *K*, equilibrium constant; *k*, rate constant; *m*/*z*, mass-to-charge ratio; MS, mass spectrometry; MT, metallothionein; NMR, nuclear magnetic resonance spectroscopy; rfMT, recombinant *F. vesiculosus* metallothionein; rhMT, recombinant human metallothionein 1a; XANES, X-ray absorption near edge structure; XAS, X-ray absorption spectroscopy.

 Published on Web 08/05/2009 

metalation reaction for many metals is very fast, the protein is oxygen sensitive, and there is a lack of good chromophores with which to monitor the progress of metalation at low concentrations and fast response times. In addition, for most reported proteins, the binding of metals in two domains results in significant complexities in the analysis of the data.

In a previous study, we reported that the arsenic−metalation reaction of metallothionein was slow enough to the isolated recombinant human α and β domains that we could determine the rate constants for the individual metalation steps for 1−3 $As^{3+}$ binding to either the α and β domains (*25*). Despite the clarity afforded by the use of the isolated domains, there have been, for many years, questions concerning the functional significance of the two domains and, particularly, whether metalation was domain specific and/or a cooperative reaction involving both domains. Studies reported by Winge et al. (*26*) have indicated that the two domains coordinate metals independently. Equilibrium data by Otvos et al. and Winge et al. show domain specificity for metals; for example, $Cu^{+}$ preferably binds the β domain, while $Cd^{2+}$ preferably binds the α domain (*27*, *28*). Maret et al. have shown that the two-domain βαMT protein is less reactive with respect to zinc transfer and thiol reactivity with disulfides than the individual domains, suggesting the two-domain structure critically affects the function of each domain (*29*). It has been reported that the efficiency and rate for the detoxification of metals are different for the isolated domains compared to the two-domain MT, which provides supporting evidence of domain interaction in native MT (*30*). Recently, we have reported the possible evolutionary advantage for a two-domain structure compared to a single-domain structure (*31*). The two-domain βα human MT binds the first metal significantly faster than a single-domain, and further, the binding rates are dependent on the number of unoccupied available binding sites; the greater number of potential sites in the βα two-domain protein resulted in much faster initial metalation.

Although there have been only a handful of studies reported in the literature that discuss the effect of the interdomain linker on the properties of MT, those previous studies have shown that both the length and the amino acid composition of the linker are important (*32*). There have been suggestions that in mammalian MT the short 2−3 amino acid linker may have some mobility (*33*) and may also enhance interdomain interactions and, hence, the metal-binding ability of MT (*34*). Huang et al. have shown that the proximity of the domains affects the stability of MT and possibly the function of MT (*18*). A longer interdomain linker is reported to reduce the stability of MT and may disrupt the interdomain interaction, thus decreasing the metal-binding ability of the protein (*18*, *34*). It is important to note that almost all metal-binding studies have been carried out on MTs with short interdomain linkers or the isolated domains. The human βαMT used in our previous As-binding studies has a linker of six residues (*31*). However, plant MTs have been reported to have much longer linkers. For example, the sequence of MT reported from the wheat *Triticum durum* has a 42 residue linker. Bilecen et al. proposed that the linker may act to elongate the structure and prevent the two domains from interacting (*17*). However, no quantitative evidence exists to account for why plant MTs have evolved such long interdomain linkers. Since several studies have suggested that the metal-binding properties of the isolated domains are not the same as the complete two-domain protein, this raises the question of whether it is the presence of the two-domain structure *per se* or whether only a two-domain structure with a short linker will exhibit the enhanced metal-binding properties.

In this study, a complete analysis is reported of the stepwise, arsenic metalation of the two-domain, 16-cysteine, recombinant *F. vesiculosus* metallothionein using temperature- (*25*, *31*, *35*) and time-resolved electrospray ionization mass spectrometry (ESI MS) (*25*, *36*−*40*). The time-resolved ESI MS data show the complete progress of the reaction from 1 $As^{3+}$ bound to 5 $As^{3+}$ bound. The data allow determination of all five, individual rate constants and the construction of a simulation that shows the progress of the metalation for the 5 $As^{3+}$ ions and the time-resolved individual occupancies of the two domains. We propose from the kinetic data that the longer length of an interdomain linker in rfMT controls the metalation properties of the two domains. The data reported here clearly show that a long interdomain linker allows the domains to bind metals independently and slower, while our previous studies show that a short interdomain linker allowed the domains to behave as a "single domain" and bind metals faster. These data represent the first report of the stepwise metalation pathway for any two-domain MT showing domain specificity prior to metal saturation.

## EXPERIMENTAL PROCEDURES

*Chemicals*. All chemicals used in this study were of the highest grade purity from commercial sources. Metal salts used were $CdSO_4$ (Fisher Scientific) and arsenic trioxide (AnalaR). Hi-Trap SP ion-exchange columns and G-25 Sephadex (Amersham Biosciences) were used for protein purification.

*Protein Preparation*. Experimental procedures have previously been reported; please refer to Ngu et al. (*25*) The recombinant *F. vesiculosus* metallothionein (rfMT) protein was based on the 67 residue sequence: MAGTG CKIWE DCKCG AACSC GDSCT CGTVK KGTTS RAGAG CPCGP KCKCT GQGSC NCVKD DCCGC GK. There are 16 cysteine residues present and no disulfide bonds. The γ domain is formed from the first seven cysteine residues starting at the N-terminus and the β domain is formed from the remaining nine cysteine residues following a 14 residue linker. In addition to the sequence from the rfMT, the expression system includes the amino acid residues of the stabilizing S-peptide tag (MKETAAAKFERQHMDSPD-LGTLVPRGS) on the N-terminus of the fragment (*41*, *42*). Previous reports have shown that the S-tag does not interfere with the reaction mechanism for binding metals in MTs (*5*, *31*, *43*). rfMT isoform 2 was expressed and purified as previously reported (*6*, *25*). The apo-rfMT protein concentrations were determined from the extinction coefficients of 148500 L $mol^{-1}$ $cm^{-1}$ at 220 nm, and the $Cd_6$-rfMT protein concentrations were determined from the extinction coefficients of 103500 L $mol^{-1}$ $cm^{-1}$ at 250 nm. The apo-rfMT concentrations for the kinetic ESI MS experiments reported here using the thermostatted mixing tee were 9.1 and 9.5 μM while the concentrations for the time-resolved ESI MS experiment were 14 and 9 μM. Oxidation is a significant problem with solutions of MT in these experiments, and the apoproteins were maintained in their reduced state by carefully deoxygenating the samples using evacuation followed by saturation with argon gas such that the proteins were sealed within an inert container. All protein samples were buffered in 25 mM ammonium formate at pH ~2.5.

*Arsenic Is a Highly Toxic Reagent* (*Caution Should Be Used When Handling Arsenic and Its Derivatives*). Solutions of 5 mM $As^{3+}$ at pH 3.5 were prepared by dissolving $As_2O_3$ (AnalaR) in concentrated HCl (Caledon) and diluting with

ultrapure deionized water (Barnstead). Aliquots of 7.4 M $NH_4OH$ (Fisher) were used to raise the pH of the $As^{3+}$ solutions. $As^{3+}$ solutions were deoxygenated and stored in a sealed inert container. Reactions were carried out at a pH range of 3−4 as this was the optimum range for product formation and stabilization; this pH was also suggested by Rey et al. (*44*) and Serves et al. (*45*) in order to stabilize the $As^{3+}$. We should mention that the structure of apo-MT in the pH range of 3−4 may be different from that observed at neutral pH, which will require further study. It has been shown that MT is located in the acidic lysosomes of kidneys (*46*, *47*), and MT immunostaining in earthworms indicates that Cd-MT is located in acidic subcellular structures similar to lysosome (*48*), making the study of $As^{3+}$ binding at low pH of interest. High salt concentrations could not be used in conjunction with the ESI MS measurements.

*ESI MS Procedures*. All data were collected using a Micromass LCT mass spectrometer in the positive ion mode. The mass spectrometer was operated using the parameters 3000.0 V capillary, 42.0 V sample cone, 22.0 V extraction cone, acquisition scan time of 4 s, and interscan delay time of 0.4 s. The ESI MS data were processed and deconvoluted using the Max Ent I software (Micromass). The instrument was calibrated using an external standard (a mixed NaI and CsI solution).

*Time-Resolved ESI MS Measurements*. Kinetic data were obtained by adding a 12× excess of $As^{3+}$ to a solution of apo-rfMT. The reactions were continuously monitored by ESI MS for up to 100 min at 23.5 ± 1 °C and 270 min at 12.6 ± 1 °C.

*Temperature-Resolved ESI MS Measurements*. Experimental procedures have previously been reported (Ngu et al. (*25*)). Kinetic data were obtained using a thermostatted mixing tee attached directly to the input capillary of the ESI MS instrument via a reaction capillary (*25*). The reaction mixing time was dependent on the length, diameter, and flow rate of the reaction capillary (*39*, *49*). The exchangeable reaction capillary had an inner diameter of 75 $\mu$m and was used with lengths ranging from 30 to 250 cm and, together with the input capillary, resulted in reaction times of 99−844 s. The fixed input capillary did affect the average temperature of the reaction at the extreme high or low temperatures and short reaction times, leading to those data sets including slightly greater uncertainties. The temperature range used was 273−350 K. Kinetic data were obtained by mixing the two streams of solutions with a flow rate of 2 $\mu$L/min for the 2.5 mM $As^{3+}$ solutions and 8 $\mu$L/min for the protein solutions, for a total flow rate of 10 $\mu$L/min, which results in a final concentration after mixing of 7.3 or 7.6 $\mu$M for rfMT and a ratio for $As^{3+}$:rfMT of 137:1 or 131:1, respectively, for the two stock protein solutions used. The temperatures reported are an average with uncertainties of ±1 K.

*Analysis of Mass Spectral Data*. The measured charge state data or the deconvoluted mass spectral data were used for the kinetic analyses. Yu et al. have shown that relative concentration of various Cd-MT species can be estimated from the relative abundances of the ions in the ESI spectrum (*36*), and this approach was previously shown to be reliable for analysis of kinetic data from human MTs (*25*, *31*). The relative abundances of all the MT species observed in each mass spectrum were summed and normalized to 100% as no internal standard was used to calibrate concentration. The sum of all MT species observed in the mass spectra was assumed to equal the concentration of the stock apo-MT solutions. In the time-resolved experiments, the relative abundances were plotted against time and fitted to calculate the $k_{n(\beta \text{ or } \gamma)}$ ($n$ = 1−3 for each step in the complete metalation reaction). In the temperature-resolved experiments, the normalized relative abundances in each spectrum, following a specific reaction mixing time, were then plotted versus $1/T$ ($K^{-1}$). As kinetic data are more readily analyzed from concentration data as a function of time at a constant temperature, our kinetic data were rearranged into this format. This serves two purposes: first, the analysis follows traditional procedures, and second, the data may be directly compared to kinetic data obtained as a function of time at a fixed temperature. In addition, the data used in the subsequent analyses are averages of many different and independent data sets, which greatly improve the confidence in the calculated results. The data sets were combined in terms of ln(relative abundance), and appropriate interpolation points were calculated for construction of three-dimensional graphs with the axes ln(relative abundance) ($y$-axis), time (s) ($z$-axis), and $1/T$ ($K^{-1}$) ($x$-axis). These 3D plots are shown in Figure 5 and Supporting Information Figure S1. From these 3D plots, slices were obtained of relative abundance as a function of time at fixed temperatures. These data sets were fitted according to Scheme 1 in order to determine the specific temperature-dependent rate constants. Finally, the reliability of the method was confirmed by back-calculating the relative abundances of all species as a function of reaction time and temperature for comparison directly with the measured data (Figure 6 and Supporting Information Figure S2).

*Minimization Method*. The deconvoluted mass spectral data provided the relative abundances for all of the MT species (*25*). Data analysis was carried out by minimization in Microsoft Excel 2003 of a series of second-order, bimolecular reactions that were part of an overall irreversible mechanism (as shown in Scheme 1). The individual distribution of $As^{3+}$ within each domain as shown in Figure 1 was calculated based on the statistical probability of the formation of each $As_n$-rfMT species. Formation of $As_5$-rfMT can occur from different metalation pathways as shown in Figure 1.

To determine the occupation of each binding site, the minimization calculation took into account the statistical probability of each species' presence. We estimate this distribution based on the relative magnitudes of the domain-specific rate constants (see Scheme 1). The rate constants were estimated and then tested against the experimental data by combining the predicted populations of the $\gamma$ and $\beta$ domains into the total $As^{3+}$ bound for the whole protein. As the analysis began with calculation of the total $As^{3+}$ bound at specific time intervals, we now have calculated the time-resolved simulation of the data actually measured. The analysis continues with iterations to improve the fit between the experimental data and the simulation by adjusting the values of the domain-specific rate constants. For example, the relative abundance of $As_1$-rfMT as measured in the mass spectrum is actually composed of two $As_1$-rfMT species: the first species contains 1 $As^{3+}$ bound in the $\beta$ domain and 0 $As^{3+}$ bound in the $\gamma$ domain ($1\beta0\gamma$ in Figure 1) while the second species contains 0 $As^{3+}$ bound in the $\beta$ domain and 1 $As^{3+}$ bound in the $\gamma$ domain ($0\beta1\gamma$ in Figure 1). The fractional occupation of these two domains ($1\beta0\gamma$ and $0\beta1\gamma$) was determined from the ratio of the individual rate constants, $k_{1\gamma}$ and $k_{1\beta}$. This process was continued for each rate constant to fill the $\beta$ and $\gamma$ domains with $As^{3+}$. The minimization was carried out by comparing the measured mass spectral data for $As_n$-rfMT ($n$ = 1−5) as shown in Figure 2 with the calculated relative abundance as a function of time. These relative abundances were calculated from each individual domain

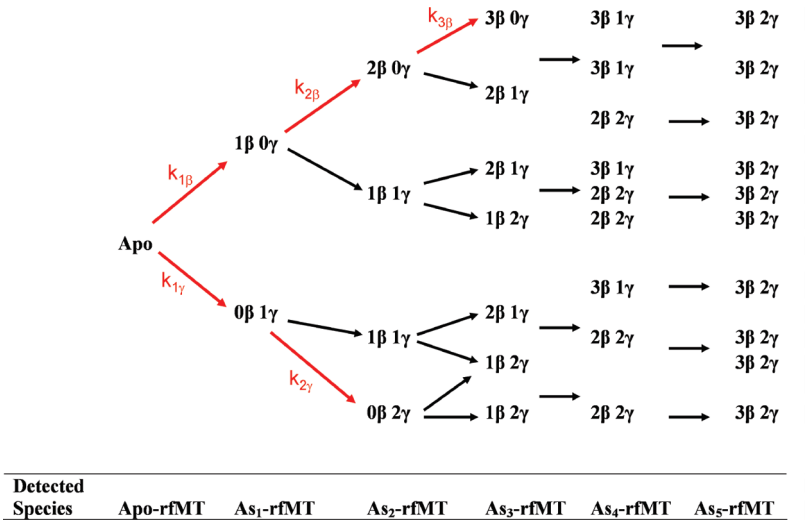


FIGURE 1: Tree diagram illustrating the different metalation pathways for the reaction of $As^{3+}$ with apo-rfMT, which result in various $As_n$-rfMT species. The reaction pathways and their associated rate constants for each domain are highlighted in red. Together, these individual steps represent the complete model in fitting the experimental data; however, the detected species shown at the bottom of the figure are observed in the ESI mass spectra. The black lines show the complexities introduced by the simultaneous metalation of both domains into the mass spectral data; hence, at each step, binding to either the $\beta$ or $\gamma$ domain is possible. The relative distribution between the two domains is directly related to the rate constants.

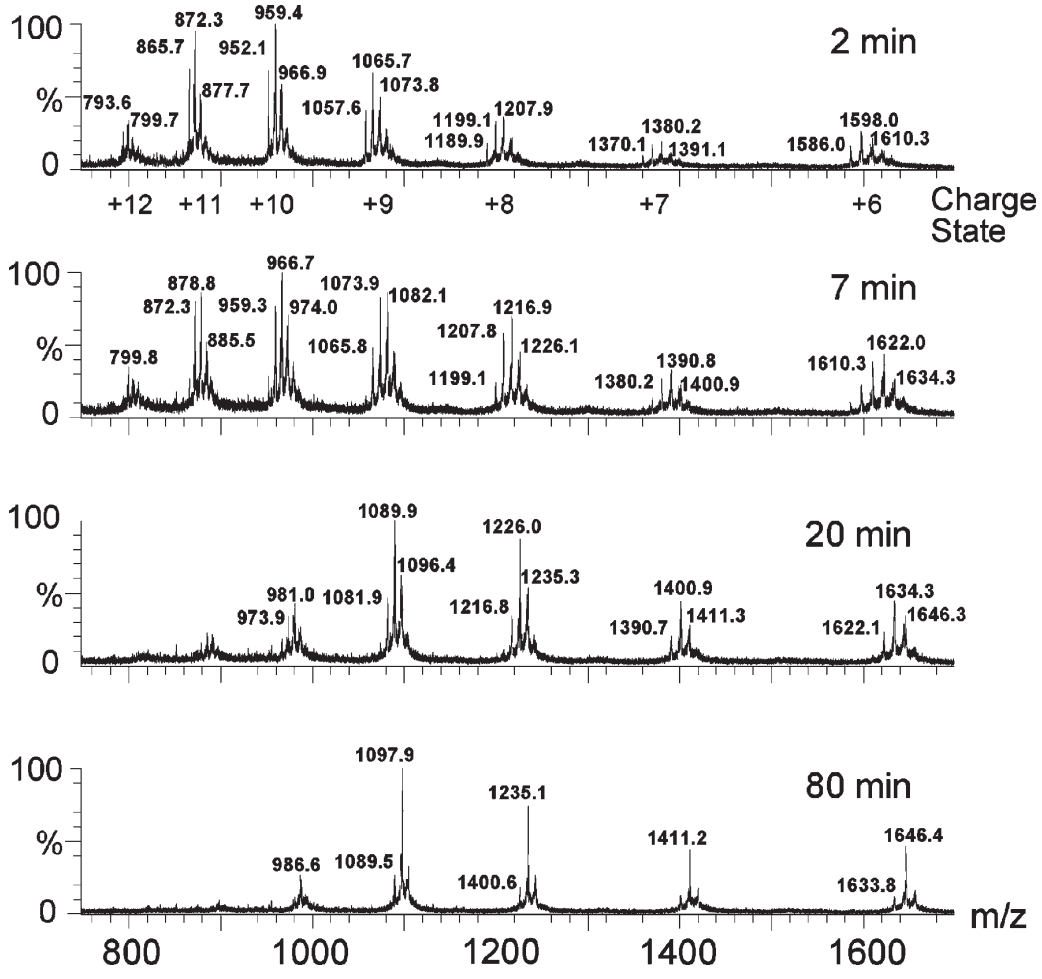


FIGURE 2: Time-resolved ESI MS for a solution of apo-rfMT (14 $\mu$M) in the presence of an $As^{3+}$ solution (261 $\mu$M) at 298 K. The charge states are shown underneath the top spectrum, and the expected $m/z$ are listed in Table 1. Each spectrum corresponds to a different reaction time (2, 7, 20, and 80 min).

species, which were determined using the calculated data. In this way the complexities of the individual time-dependent occupation of the domains by $As^{3+}$, as shown in Figure 1, were reduced to the time-dependent relative abundances of a series of 5 $As^{3+}$-containing protein species, which were the same as measured experimentally. This was required because the domains in rfMT behaved independently even though they were part of the same protein unlike our previous analyses (*25*, *31*).

## RESULTS

ESI MS data were obtained continuously for up to 80 min following mixing of 261 $\mu$M $As^{3+}$ with 14 $\mu$M apo-rfMT. Figure 2 shows the progress of the metalation reaction at five fixed time points (2, 7, 20, and 80 min) over the 80 min reaction. The ESI MS data were measured at mass units related to the mass/charge of the ion. For proteins, the charge is usually far greater than +1, and many different charged species coexist in equilibrium. An increase in the envelope charge state maximum is considered to be a result of increased exposure of the protonatable basic side chains in the protein due to an increase in volume of the protein.

Scheme 1: Sequential Binding Mechanism Proposed for $As^{3+}$ Binding to the $\gamma$ (A) and $\beta$ (B) Domains of rfMT[a]

Scheme A – γrfMT

$$H_7\text{-}\gamma\text{rfMT} + As^{3+} \xrightarrow{k_{1\gamma}} As_1\text{-}H_4\text{-}\gamma\text{rfMT} + 3H^+$$
$$As_1\text{-}H_4\text{-}\gamma\text{rfMT} + As^{3+} \xrightarrow{k_{2\gamma}} As_2\text{-}H_1\text{-}\gamma\text{rfMT} + 3H^+$$

Scheme B – βrfMT

$$H_9\text{-}\beta\text{rfMT} + As^{3+} \xrightarrow{k_{1\beta}} As_1\text{-}H_6\text{-}\beta\text{rfMT} + 3H^+$$
$$As_1\text{-}H_6\text{-}\beta\text{rfMT} + As^{3+} \xrightarrow{k_{2\beta}} As_2\text{-}H_3\text{-}\beta\text{rfMT} + 3H^+$$
$$As_2\text{-}H_3\text{-}\beta\text{rfMT} + As^{3+} \xrightarrow{k_{3\beta}} As_3\text{-}\beta\text{rfMT} + 3H^+$$

[a]The rate constants for each step are indicated by $k_{1,2,3(\gamma \text{ or } \beta)}$, which are for the rate of adding a single $As^{3+}$ to the metallothionein domain to form a product with $n$ (1, 2, or 3) $As^{3+}$ bound. This same nomenclature is used in the text where the experimental values are reported.

Table 1: Calculated Mass and Mass/Charge for $As^{3+}$-Metalated rfMT Species Based on the Primary Amino Acid Sequence of rfMT

| | | charge state and predicted $m/z$ for each species | | | | | | |
|---|---|---|---|---|---|---|---|---|
| | mass (Da) | +6 | +7 | +8 | +9 | +10 | +11 | +12 |
| apo-rfMT | 9512.1 | 1586.3 | 1359.9 | 1190.0 | 1057.9 | 952.2 | 865.7 | 793.7 |
| $As_1$-rfMT | 9584.0 | 1598.3 | 1370.1 | 1199.0 | 1065.9 | 959.4 | 872.3 | 799.7 |
| $As_2$-rfMT | 9655.9 | 1610.3 | 1380.4 | 1208.0 | 1073.9 | 966.6 | 878.8 | 805.7 |
| $As_3$-rfMT | 9727.8 | 1622.3 | 1390.7 | 1217.0 | 1081.9 | 973.8 | 885.3 | 811.6 |
| $As_4$-rfMT | 9799.7 | 1634.3 | 1401.0 | 1226.0 | 1089.9 | 981.0 | 891.9 | 817.6 |
| $As_5$-rfMT | 9871.6 | 1646.3 | 1411.2 | 1234.9 | 1097.8 | 988.2 | 898.4 | 823.6 |

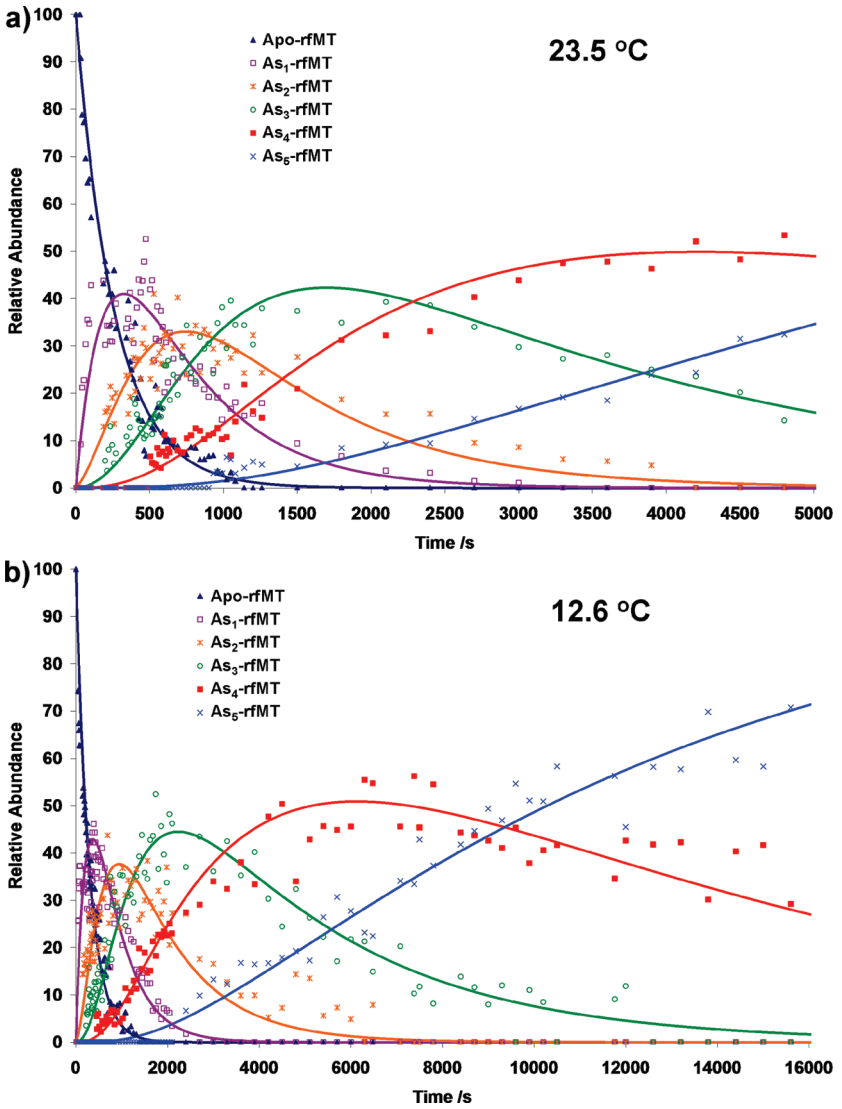


FIGURE 3: Time-resolved, experimental relative abundances for apo-rfMT and $As_n$-rfMT ($n$ = 1−5) following reaction of 9 $\mu$M apo-rfMT with 108 $\mu$M $As^{3+}$ at 23.5 and 12.6 °C. The legend identifies the time course of the abundances for each mass (symbols). The lines were calculated based on minimization of the parameters in the complete analysis of the kinetic data for the relative abundance at each of the specified times using the series of sequential bimolecular reactions shown in Scheme 1. The method is described in the text. The experiment data have a percent standard error of 7%.

Using Table 1, we can identify in Figure 2 all of the rfMT species present. In Figure 2, at the 2 min point, the +10 and +11 charge states are maximal, but all of the charge states from +6 to +12 arise from the apo-rfMT, which has a mass of 9512.1 Da. Figure 2 shows that there is a shift in the dominant charge states from +10/+11 for apo-rfMT to +8/+9 for $As_5$-rfMT, which suggests a less solvent accessible structure for the fully As-metalated species. It is clear from the time-dependent MS data in Figure 2 that all six species, that is, apo-rfMT to $As_5$-rfMT, coexist and that over time the $As_5$-rfMT species predominates.

Unlike the pathway for $As^{3+}$ metalation of the single $\beta$ or α domain of human MT (*25*) or the human two-domain $\beta\alpha$MT (*31*), the ESI MS data for the two-domain rfMT are much more complicated because, we propose, the data represent the combination of all metalation products for both domains. Difficulties arise when in the determination of the actual metal ion distribution within each domain as a function of time before all sites are saturated. Prior to all five sites being filled, the MS data simply show the total mass of the $As^{3+}$ summed over both domains with no indication of the individual location of the incoming $As^{3+}$. However, it is clear that the distribution into each domain (the 9-cysteine $\beta$ and the 7-cysteine $\gamma$ domain) is controlled by the individual rate constants for the bimolecular reactions as shown in Scheme 1.

The mechanism for the metalation pathway was determined by analysis of the kinetic data sets for the reactions of a solution of 9 $\mu$M apo-rfMT mixed with 108 $\mu$M $As^{3+}$, which gives an $As^{3+}$:MT stoichiometric ratio of 12:1 measured at 285.7 and 296.7 K. The measured charge state data were deconvoluted into the time-resolved relative abundances for apo-rfMT and $As_n$-rfMT ($n = 1-5$) (Figure 3). Each symbol in Figure 3 represents the abundance of a single mass that is associated with a specific metalated species, as shown in the legend.

As there are two domains, there is ambiguity at this stage concerning the distribution of the $As^{3+}$ between the domains. The data were fitted to the five bimolecular reactions shown in Scheme 1, using the summation of the statistical probability for the presence of each species present with that mass and the resulting predicted occupation of each domain from the individual rate constants. Thus, the theoretical lines were calculated from analysis of data sets measured at all reaction times to obtain the specific rate constants, $k_n$, which were used with the experimental concentrations of the protein and the $As^{3+}$ to predict the concentration of each species at the specified time. The lines in Figure 3 show the results of the fit but do not at this point show the occupancy of the individual domain; rather the lines in Figure 3 fit the experimentally determined data and, therefore, simulate the total number of $As^{3+}$ ions that have bound to the protein, from zero (for apo-rfMT) to five (for the saturated $As_5$-rfMT). The complication caused by simultaneous occupation of both domains can be seen from this example: $As_3$-rfMT (the "○" in Figure 3) is measured as a single species in the ESI mass spectrum even though it may be composed of (i) 0 $As^{3+}$ in $\gamma$ and 3 $As^{3+}$ in $\beta$ or (ii) 1 $As^{3+}$ in $\gamma$ and 2 $As^{3+}$ in $\beta$ or (iii) 2 $As^{3+}$ in $\gamma$ (the maximum occupation for $\gamma$) and 1 $As^{3+}$ in $\beta$. It is important to note that all of the lines in Figure 3 are interconnected, and adjustment of the value of any single rate constant in Scheme 1 affects the outcome of the fit for all of the As-rfMT species.

The kinetic parameters, which were determined following minimization of the mechanism in Scheme 1 with five different rate constants, provided all of the parameters necessary to

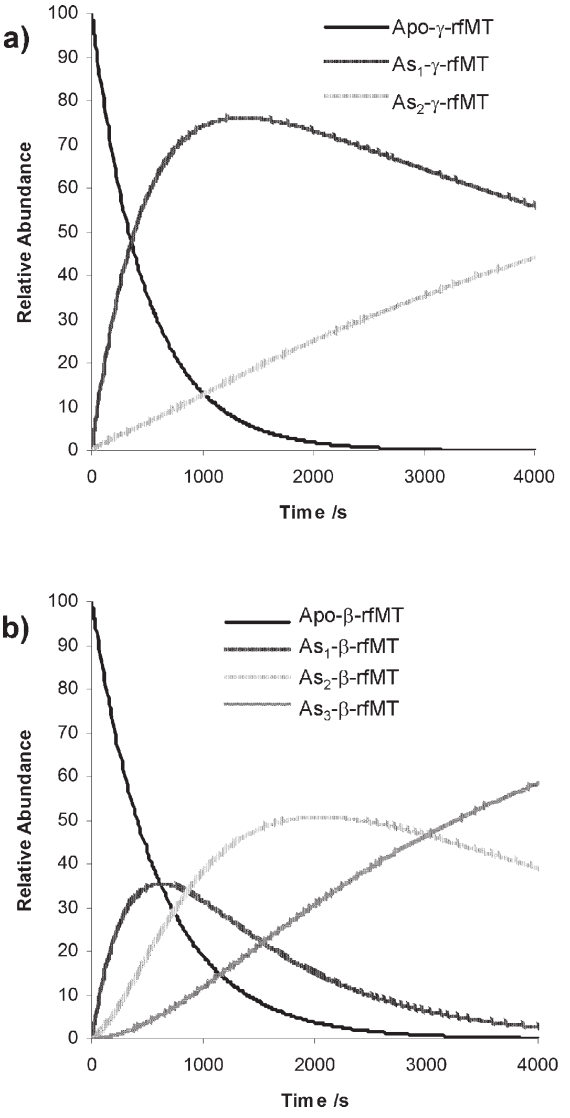


FIGURE 4: Simulation of the sequential binding mechanism shown in Scheme 1 for $As^{3+}$ binding to the $\gamma$-rfMT (a) and $\beta$-rfMT (b) domains over 4000 s. Time dependences of the fractional concentrations are plotted as the relative abundances of the protein species that form following mixing of 9 $\mu$M apo-rfMT with 108 $\mu$M $As^{3+}$ at 23.5 °C using the rate constants reported in the text. Modeled based on an $As^{3+}$:rfMT ratio of 12:1.

determine the individual domain distributions of $As^{3+}$ during the metalation reaction, as is shown in Figure 4. Figure 4 provides a simulation of the metalation of the individual $\gamma$ and $\beta$ domains taking place simultaneously in the two-domain protein. Combining the relative abundance of each species in Figure 4 and taking into account the probability of the distribution of $As^{3+}$ between the two domains gives the observed ESI MS data in Figure 3. The rate constants ($M^{-1}$ $s^{-1}$) at 298 K calculated from the fits for the $\gamma$ domain are $k_{1\gamma}$, 19.8, and $k_{2\gamma}$, 1.4, and for the $\beta$ domain are $k_{1\beta}$, 16.3, $k_{2\beta}$, 9.1 and $k_{3\beta}$, 2.2 (Figure 3). The rate constants ($M^{-1}$ $s^{-1}$) at 286 K calculated from the fits for the $\gamma$ domain are $k_{1\gamma}$, 11.3, and $k_{2\gamma}$, 0.6, and for the $\beta$ domain are $k_{1\beta}$, 9.7, $k_{2\beta}$, 4.0, and $k_{3\beta}$, 1.1 (Figure 3). We should emphasize that the data in Figure 4 are different from the fits in Figure 3 because the lines in Figure 3 are derived from the statistical average of all species shown in Figure 4 at any one time that give a specific mass.

The results of the analysis shown in Figure 4 indicate that each domain of rfMT binds the $As^{3+}$ ions independently in a series of

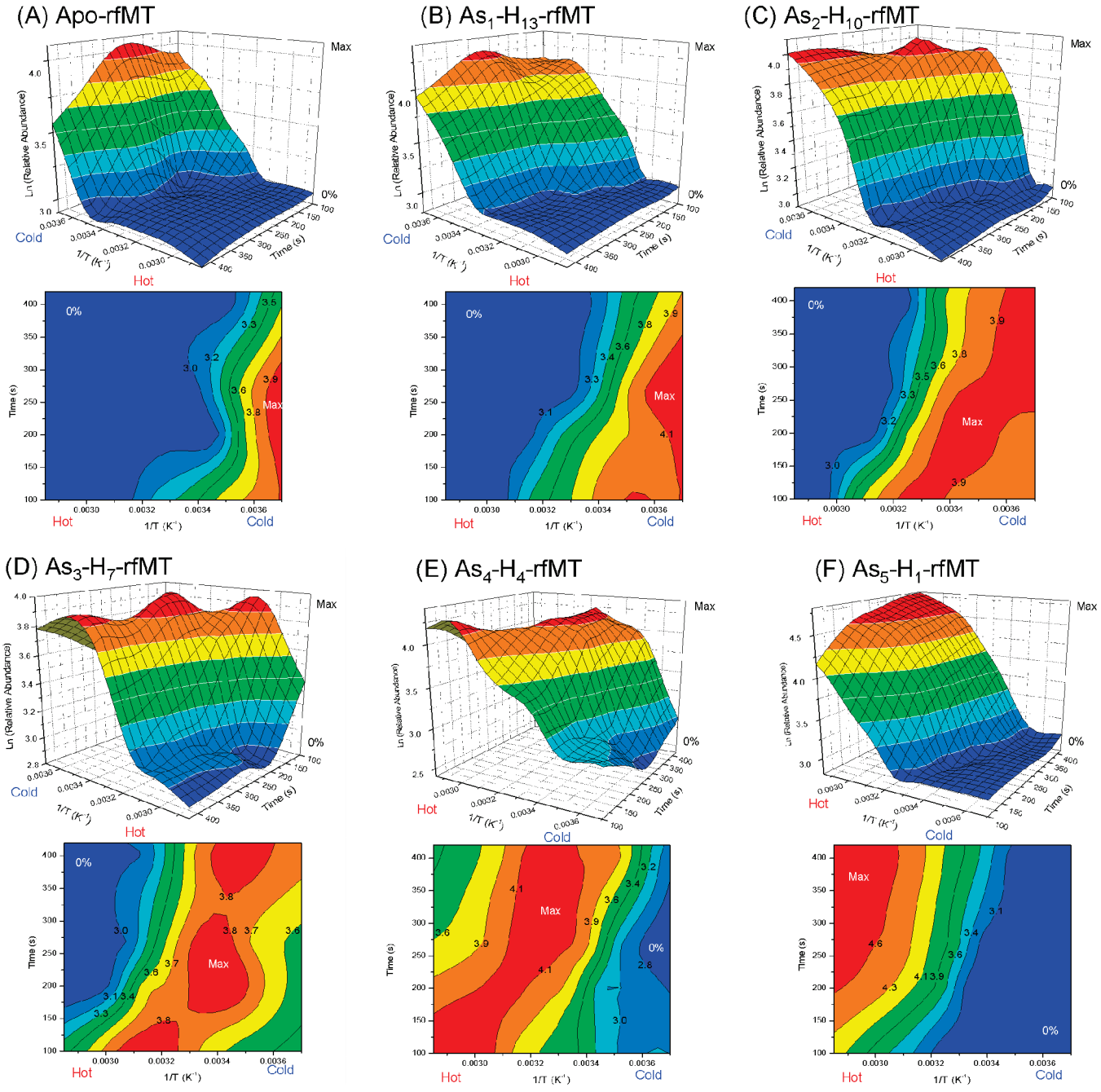


FIGURE 5: Trends in concentrations of the individual $As_n$-rfMT ($n = 0-5$) species as a function of temperature, $1/T$ ($K^{-1}$), and time following mixing apo-rfMT with $As^{3+}$. The diagrams were constructed from a series of ESI MS traces recorded between 273 and 346 K, and for reaction times between 102 and 402 s, from different solutions each with an $As^{3+}$:rfMT stoichiometric ratio of 131:1 with solutions containing 7.6 $\mu$M apo-rfMT and 2.5 mM $As^{3+}$. (Top) 3D visualization of ln(relative abundance) versus $1/T$ and reaction time (on the $z$-axis) for a single component species extracted from the total reaction. (Bottom) Contour diagrams calculated from the 3D plots. It is important to note that to aid visualization and clarity of the trend in concentration as a function of time and temperature each 3D plot has been orientated so that the 0% relative abundance of the specific species is at the front. For example, for apo-rfMT (A) and $As_{1-3}$-rfMT (B−D), the conditions for 0% relative abundances are high temperatures and long reaction times, and the 3D plots are orientated such that high temperatures and long reaction times are at the front. The contour diagrams provide more detail of the reaction profiles.

two (for $\gamma$) and three (for $\beta$) sequential bimolecular reactions. There is no indication of cooperativity in the metalation reactions of each individual domain; that is, each of the stepwise species form in sequence rather than predominantly forming the final product, $As_3$-$\beta$-domain or $As_2$-$\gamma$-domain, at the expense of the partially metalated species.

We have previously shown that $As^{3+}$ metalation of human MT is temperature- and time-dependent (*31*, *50*). Further, using the ESI mass spectrometer and a thermostatted mixing tee, we have shown that it was possible to measure the time, temperature, and concentration dependence of the reaction of $As^{3+}$ with MT and extract the activation energies and Arrhenius factors for each step (*31*, *50*). In this current study, the kinetic data were determined for the $As^{3+}$ metalation of the more complex, two-domain rfMT protein for a series of fixed reaction times at a range of temperatures.

Figure 5 shows the 3D representation of the relative concentrations of each As species in the metalation of apo-rfMT with $As^{3+}$ from $As_1$-$H_{13}$-rfMT to $As_5$-$H_1$-rfMT as a function of time and temperature using the temperature-resolved ESI MS data.

Table 2: Rate Constants, Activation Energies ($E_A$), Arrhenius Factor ($A$), Activation Enthalpies ($\Delta H^{\ddagger}$), Activation Entropies ($\Delta S^{\ddagger}$), and Activation Free Energies ($\Delta G^{\ddagger}$) for the $As^{3+}$-Induced Metalation of rfMT at pH 3.5

| arsenic species formed | $n^a$ | $k_n{}^a$ at 298 K/$M^{-1}$ $s^{-1}$ | $E_A{}^b$/kJ $mol^{-1}$ | $A/10^{-5}$ $M^{-1}$ $s^{-1}$ | $\Delta H^{\ddagger}$/kJ $mol^{-1}$ | $\Delta S^{\ddagger}$/J $K^{-1}$ $mol^{-1}$ | $\Delta G^{\ddagger}$ at 298 K/kJ $mol^{-1}$ |
|---|---|---|---|---|---|---|---|
| $As_1$-$H_4$-$\gamma$rfMT[c] | $1\gamma$ | 19.8 | 34 | 231 | 32 | −112 | 65 |
| $As_2$-$H_1$-$\gamma$rfMT | $2\gamma$ | 1.4 | 33 ± 14 | 9.2 ± 4 | 31 ± 14 | −138 ± 115 | 72 ± 69 |
| $As_1$-$H_6$-$\beta$rfMT[c] | $1\beta$ | 16.3 | 32 | 62 | 29 | −123 | 66 |
| $As_2$-$H_3$-$\beta$rfMT | $2\beta$ | 9.1 | 35 ± 9 | 77 ± 18 | 33 ± 9 | −121 ± 49 | 69 ± 34 |
| $As_3$-$\beta$rfMT | $3\beta$ | 2.2 | 27 ± 7 | 1.6 ± 0.4 | 25 ± 6 | −153 ± 81v | 71 ± 42 |
| average | | N/A | 32 ± 1 | N/A | 30 ± 1 | 129 ± 7 | 69 ± 1 |

[a]For reactions as shown in Scheme 1, where $k_n$ refers to the rate constant for a single step that involves addition of a single $As^{3+}$ forming a product with $n$ $As^{3+}$ bound. Each rate constant has a percent standard error of ±7%. [b]A temperature range of 270−350 K and 51 data points were used to construct the 3D plots that generated these activation parameters. [c]Due to the very fast reaction, data could not be obtained for a wide range of temperatures. The data for $k_{1(\beta \text{ and } \gamma)}$ were estimated from only two data sets.

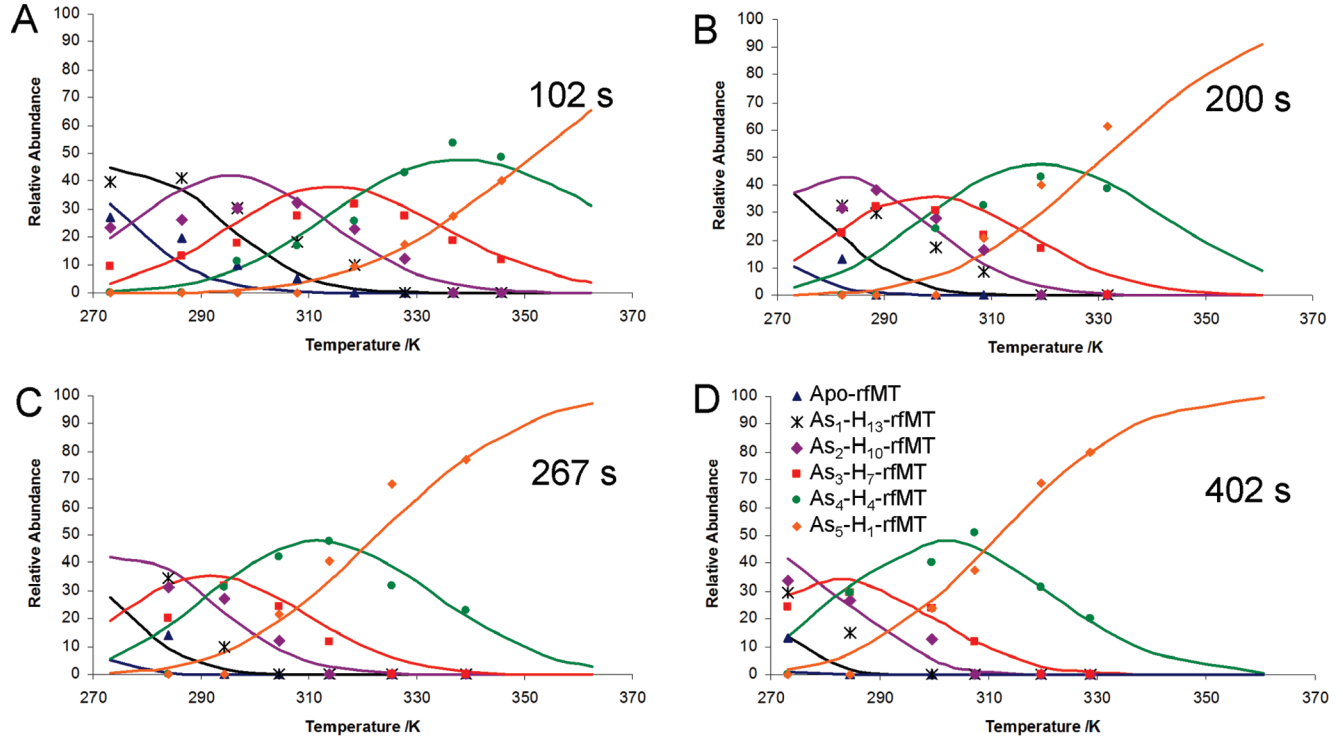


FIGURE 6: Temperature-resolved relative abundances of apo-rfMT and $As_n$-rfMT ($n$ = 1−5) following reaction of apo-rfMT with $As^{3+}$ at fixed reaction times. ESI MS data were obtained for apo-rfMT at a series of fixed reaction times with increasing temperatures (273−346 K) in the presence of excess $As^{3+}$. The fixed reaction times were 102 s (A), 200 s (B), 267 s (C), and 402 s (D). The reaction was carried out with an $As^{3+}$:rfMT stoichiometric ratio of 131:1 with solutions containing 7.6 $\mu$M apo-rfMT and 2.5 mM $As^{3+}$. The smooth lines were calculated based on the complete analysis of the kinetic data for the relative abundance of each component species for every set temperature at the specified times. The lines are connected by a series of five sequential reactions shown in Scheme 1 and described in the text. The data points that comprise the theoretical lines were calculated from analysis of data sets measured at all reaction times and temperatures to obtain the kinetic parameters, $k_{temp}$, $A$, and $E_A$, which were used with the experimental concentrations of the protein and the $As^{3+}$ to predict the concentration of each species at the specified temperature and time. There will always be considerable uncertainty in any simulation that uses parameters extracted from the entire temperature−time-relative abundance data set which is comprised of many different experiments.

Contour plots are also included in Figure 5. Multiple data sets of the reaction concentrations during a set time course were extracted at a range of reaction temperatures from the 3D plots and analyzed using the reaction mechanism in Scheme 1. The temperature-dependent rate constants were calculated and plotted as ln($k$) versus 1/$T$ (Supporting Information Figure S3A) and ln($k$/$T$) versus 1/$T$ (Supporting Information Figure S3B) to evaluate activation energies, Arrhenius factors, and the Eyring transition state parameters listed in Table 2.

To test the validity of our method and the accuracy of the parameters listed in Table 2, we have simulated the relative abundance for each $As_n$-rfMT species ($n$ = 0−5) for every data point measured during the temperature-resolved experiments (Figure 6). The smooth lines in Figure 6 are simulations of the five bimolecular reactions occurring over the range of reaction times and temperatures shown. The simulations are reliant on the specific temperature-dependent rate constants calculated from the stepwise activation energies and Arrhenius constants, $A$, shown in Table 2. In view of the inherent difficulties involved in these temperature- and time-dependent experiments, we believe that the fits of the data are remarkably good. In Figure 6A, it is clear that at the 102 s reaction time and at cool temperatures the dominant species are apo- and $As_{1-2}$-rfMT; however, at the same reaction time but at higher temperatures, the dominant species are $As_{4-5}$-rfMT, clearly showing that the reaction progresses more rapidly at higher temperatures. The same trend is observed for all other reaction times (Figure 6B−D).

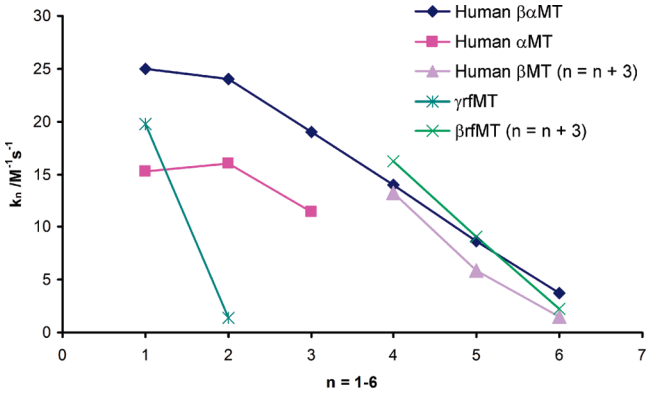


FIGURE 7: Comparison of the rate constants calculated from the time-resolved ESI MS measurements for $As^{3+}$ metalation of αhMT, βhMT, βαhMT (*31*), γrfMT, and βrfMT. The rate constant data for βhMT and βrfMT were drawn with the value of $n$ shifted by 3 to illustrate the similarity to the rate constant trend of the final three $As^{3+}$ binding to βαhMT.

## DISCUSSION

The seaweed *F. vesiculosus* metallothionein protein represents an unusual member of a group of MTs where the two domains are connected by a long interdomain linker. This atypical group of MTs, when compared to mammalian MTs, is often observed in MTs from plant and algae (*3*, *9*, *10*). This present report details the first complete metalation pathway for any metal binding to a plant or algal MT. The use of ESI MS data allowed for the observation of all of the As-containing species present. Statistical probability analysis based on the individual specific rate constants and metal-domain occupation allowed for modeling of the metal distribution within the individual domains. While the multiple metalation of the two-domain MT proteins is unique, many other proteins with two metal-binding domains likely undergo similar metalation reactions, the mechanisms of which can now be analyzed using the methodology discussed here.

*Mechanism of $As^{3+}$ Metalation of rfMT*. Our recent studies of the two-domain human MT suggest that the $As^{3+}$ binds first in the α and then in the β domain during the metalation. The analysis of the time-resolved ESI MS studies for rfMT reported here show that both the γ and the β domains bind the first $As^{3+}$ almost simultaneously. The mechanism in Scheme 1 describes the binding of $As^{3+}$ to the two domains of rfMT as two essentially independent reaction pathways and where the rate law for each bimolecular reaction step is rate = $k_n[As_{n-1}MT][As^{3+}]$.

The presence of intermediates validated the assumption of a sequential rather than a cooperative reaction mechanism. The sequential mechanism and the lack of evidence showing thiolate bridging (as there are unbound cysteines in the γ domain) suggest that there is no cluster formation with respect to $As^{3+}$. The ESI mass spectra in Figure 2 show that the difference in mass between As-MT peaks corresponds to approximately one As atom minus three protons. Previous reports have proposed that each $As^{3+}$ is coordinated to three cysteinyl sulfurs in a distorted trigonal pyramidal geometry (*25*, *31*, *51*, *52*).

*Comparison and Implications of the Rate Constants*. The kinetic data listed in Table 2 clearly show that the rate constant values systematically decrease with each additional $As^{3+}$ bound for metalation of the 7-cysteine γ domain and the 9-cystene β domain, indicating noncooperative binding, which correlates well with our previous reports (*25*, *31*). The values for $k_{1\beta}$ and $k_{1\gamma}$ are too similar; thus we cannot suggest any significant reason for $k_{1\gamma}$ being greater than $k_{1\beta}$.

Figure 7 compares the rate constant values for rfMT with those of human MT. The rate constants, $k_{1-3\beta}$ for βrfMT and $k_{1-3\beta}$ for human βhMT, are shown shifted by $n = 3$ places to align them with $k_{4-6\beta\alpha}$ for human βαMT; this emphasizes the relative closeness of these values to each other. On the basis of the similarities between the rate constant values for the β domain in human MT and rfMT, we can see that the 9-cysteine β domain metalates similarly for the different species of MTs.

Overall, the metalation of the two-domain rfMT is much slower than the two-domain human βαhMT. In fact, the rate constant values observed for rfMT are reminiscent of the rate constant values observed for the individual β and α domain fragments for human MT. We have proposed in our previous report that the two-domain βα human MT binds the first metal faster compared with a single-domain MT because the two-domain protein has a greater number of available and equivalent binding sites (*31*). Given that the domains in rfMT are binding $As^{3+}$ independently of each other, it is not surprising the rate constants for the individual domains are slower as there are fewer identical binding sites.

*Implications of the Values of the Kinetic and Eyring Transition State Parameters*. Table 2 lists the activation energies for the reaction forming $As_n$-rfMT ($n = 1-5$). Supporting Information Figure S3 shows the Arrhenius plot and Eyring plot for the $k_{1-2\gamma}$ and $k_{1-3\beta}$. The activation energies are similar for the formation of each $As_n$-rfMT ($n = 1-5$) shown in Table 2, while the Arrhenius factor is generally decreasing. We conclude, therefore, that the Arrhenius factor (the statistical frequency of collisions that result in product formation) is controlling the rate of the $As^{3+}$ metalation reaction.

$\Delta H^{\ddagger}$, $\Delta S^{\ddagger}$, and $\Delta G^{\ddagger}$ correspond to those calculated by Ngu et al. (*25*, *31*) and provide further confirmation that the underlying chemistry for $As^{3+}$ metalation of rfMT is similar to that observed in human metallothionein.

*Comments on the Metalation of Multiple Domain Proteins*. Metalloproteins may contain multiple metal-binding domains, and these domains may have different reactivities. Studying these multidomain metalloproteins can be challenging when one is unable to accurately predict which domain is reacting. The results described in this report demonstrate that domain-specific metalation information can be obtained from a two-domain protein where the instrumentation cannot discern domain specificity by applying the statistical probabilities of the occupation of each domain by the incoming metal. The As-rfMT species observed by the ESI MS are controlled by the relative abundance of each As species per domain, which are in turn controlled by the individual domain rate constants, for example, $k_{1\beta}$.

*The Role of the Interdomain Linker*. In mammalian MTs, the interdomain linker is only a few amino acids long (*53*, *54*); however, in plant MTs, the interdomain linker can be much longer (*10*, *17*). Studies on wheat *T. durum* MT have reported that the protein is a two-domain protein connected by 42 amino acid interdomain linker (*17*). The sequence of the interdomain linker has been found to be conserved among plants. Homology modeling and *ab initio* calculations of the wheat *T. durum* MT suggest that the interdomain linker may have both a structure and a function (*17*). An interesting study that focused on changing the interdomain linker length showed that increasing

the length of the interdomain linker could add flexibility to MT's rather compact structure and that the domains remain functional after the interdomain space is perturbed (*18*).

A major result of the analysis of the ESI MS data in this report is that the two domains in rfMT act independently when binding $As^{3+}$, whereas studies of $As^{3+}$ metalation of recombinant human βαMT show that the two domains in that protein interact during metalation (*31*). This difference in behavior between the two species of MT is surprising but may be explained by the difference in the length of the interdomain linker. The recombinant human βαMT protein we used in our previous report had a linker that was 6 residues long (*31*) compared to the 14 residues in the rfMT. We believe that the increase in interdomain space for rfMT compared to human MT allows the domains in rfMT to act independently of each other when the protein metalates. This also suggests that there may be a critical length between 6 and 14 amino acids where a transition in domain behavior occurs. We can speculate, based on the kinetic data, that the short interdomain linker in MT represents an evolutionary enhancement for species where cellular metal concentrations have to be maintained at very low levels. As with the report of the trend in the rate constant values as a function of $As^{3+}$ bound for the βα human MT, we suggest that these new kinetic data provide quantitative information concerning the metalation properties of MTs in general that have previously been unavailable.

## CONCLUSIONS

The analysis of the ESI MS data provides values for all five rate constants, allowing a complete description of the reaction in which $As^{3+}$ binds to rfMT. The five individual rate constants are shown for the mechanism in Scheme 1 to control the location of the individual $As^{3+}$ ions. These are the first data that describe the stepwise metalation of a two-domain metallothionein showing domain specificity, which clearly shows the importance of the interdomain linker in controlling MT's behavior with respect to the rate of metalation and to the overall domain-specific mechanism.

## ACKNOWLEDGMENT

We thank Prof. R. J. Puddephatt for use of the Micromass LCT-ESI MS funded by the Canada Research Chair program. We are grateful to the Department of Biochemistry, University of Western Ontario, for use of the cell culture equipment.

## SUPPORTING INFORMATION AVAILABLE

Three figures (S1−S3) with descriptive text that show the second set of data used in the experiments, the Arrhenius plot, and the Eyring plot referred to in the text. This material is available free of charge via the Internet at http://pubs.acs.org.

## REFERENCES

1. Hug, S., Wegelin, M., Gechter, D., and Canonica, L. (2000) Arsenic contamination of ground water: disastrous consequences in Bangladesh. *EAWAG News 49*, 18–20.
2. Mead, M. N. (2005) Arsenic. In search of an antidote to a global poison. *Environ. Health Perspect. 113*, A378–A386.
3. Morris, C. A., Nicolaus, B., Sampson, V., Harwood, J. L., and Kille, P. (1999) Identification and characterization of a recombinant metallothionein protein from a marine alga, *Fucus vesiculosus*. *Biochem. J. 338*, 553–560.
4. Singh, S., Mulchandani, A., and Chen, W. (2008) Highly selective and rapid arsenic removal by metabolically engineered *Escherichia coli* cells expressing *Fucus vesiculosus* metallothionein. *Appl. Environ. Microbiol. 74*, 2924–2927.
5. Merrifield, M. E., Chaseley, J., Kille, P., and Stillman, M. J. (2006) Determination of the Cd/S cluster stoichiometry in *Fucus vesiclosus* metallothionein. *Chem. Res. Toxicol. 19*, 365–375.
6. Merrifield, M. E., Ngu, T., and Stillman, M. J. (2004) Arsenic binding to *Fucus vesiculosus* metallothionein. *Biochem. Biophys. Res. Commun. 324*, 127–132.
7. Margoshes, M., and Vallee, B. L. (1957) A cadmium protein from equine kidney cortex. *J. Am. Chem. Soc. 79*, 4813.
8. Stillman, M. J., Shaw, C. F., III, and Suzuki, K. T. (1992) Metallothioneins , 1st ed., VCH Publishers, New York.
9. Suzuki, K. T., Imura, N., and Kimura, M. (1993) Metallothionein III , Vol. 3, 1st ed., Birkhauser, Boston, MA.
10. Robinson, N. J., Tommey, A. M., Kuske, C., and Jackson, P. J. (1993) Plant metallothioneins. *Biochem. J. 295*, 1–10.
11. Otvos, J. D., and Armitage, I. M. (1980) Structure of the metal clusters in rabbit liver metallothionein. *Proc. Natl. Acad. Sci. U.S.A. 77*, 7094–7098.
12. Boulanger, Y., Armitage, I. M., Miklossy, K.-A., and Winge, D. R. (1982) $^{113}$Cd NMR study of a metallothionein fragment: evidence for a two-domain structure. *J. Biol. Chem. 257*, 13717–13719.
13. Cobbett, C., and Goldsbrough, P. (2002) Phytochelatins and metallothioneins: roles in heavy metal detoxification and homeostasis. *Annu. Rev. Plant Biol. 53*, 159–182.
14. Robinson, N. J. (1989) Algal metallothioneins: secondary metabolites and proteins. *J. Appl. Phycol. 1*, 5–18.
15. Domenech, J., Mir, G., Huguet, G., Capdevila, M., Molinas, M., and Atrian, S. (2006) Plant metallothionein domains: functional insight into physiological metal binding and protein folding. *Biochimie 2006*, 583–593.
16. Peroza, E. A., and Freisinger, E. (2007) Metal ion binding properties of *Tricium asetivum* $E_c$-1 metallothionein: evidence supporting two separate metal thiolate clusters. *J. Biol. Inorg. Chem. 12*, 377–391.
17. Bilecen, K., Ozturk, U. H., Duru, A. D., Sutlu, T., Petoukhov, M. V., Svergun, D. I., Koch, M. H. J., Sezerman, U. O., Cakmak, I., and Sayers, Z. (2005) *Triticum durum* metallothionein. *J. Biol. Chem. 280*, 13701–13711.
18. Rhee, I.-K., Lee, K. S., and Huang, P. C. (1990) Metallothioniens with interdomain hinges expanded by insertion mutagenesis. *Protein Eng. 3*, 221–226.
19. Pattanaik, A., Bachowski, G., Laib, J., Lemkuil, D., Shaw, C. F.III, Petering, D. H., Hitchcock, A., and Saryan, L. (1992) Properties of the reaction of *cis*-dichlorodiammineplatinum(II) with metallothionein. *J. Biol. Chem. 267*, 16121–16128.
20. Salgado, M. T., and Stillman, M. J. (2004) $Cu^+$ distribution in metallothionein fragments. *Biochem. Biophys. Res. Commun. 318*, 73–80.
21. Ejnik, J., Robinson, J., Zhu, J., Forsterling, H., Shaw, C. F.III, and Petering, D. H. (2002) Folding pathway of apo-metallothionein induced by $Zn^{2+}$, $Cd^{2+}$ and $Co^{2+}$. *J. Inorg. Biochem. 88*, 144–152.
22. Rigby Duncan, K. E., and Stillman, M. J. (2007) Evidence for noncooperative metal binding to the α domain of human metallothionein. *FEBS J. 274*, 2253–2261.
23. Blindauer, C. A., Polfer, N. C., Keiper, S. E., Harrison, M. D., Robinson, N. J., Langridge-Smith, P. R. R., and Sadler, P. J. (2003) Inert site in a protein zinc cluster: isotope exchange by high resolution mass spectrometry. *J. Am. Chem. Soc. 125*, 3226–3227.
24. Krezel, A., and Maret, W. (2007) Dual nanomolar and picomolar Zn(II) binding properties of metallothionein. *J. Am. Chem. Soc. 129*, 10911–10921.
25. Ngu, T. T., and Stillman, M. J. (2006) Arsenic binding to human metallothionein. *J. Am. Chem. Soc. 128*, 12473–12483.
26. Nielson, K. B., and Winge, D. R. (1985) Independence of the domains of metallothionein in metal binding. *J. Biol. Chem. 260*, 8698–8701.
27. Li, H., and Otvos, J. D. (1996) $^{111}$Cd NMR studies of the domain specificity of $Ag^+$ and $Cu^+$ binding to metallothionein. *Biochemistry 35*, 13929–13936.
28. Nielson, K. B., and Winge, D. R. (1984) Preferential binding of copper to the β domain of metallothionein. *J. Biol. Chem. 259*, 4941–4946.
29. Jiang, L.-J., Vasak, M., Vallee, B. L., and Maret, W. (2000) Zinc transfer potential of the α- and β-clusters of metallothionein are affected by domain interactions in the whole molecule. *Proc. Natl. Acad. Sci. U.S.A. 97*, 2503–2508.
30. Capasso, C., Carginale, V., Crescenzi, O., Di Maro, D., Spadaccini, R., Temuss, P. A., and Parisi, E. (2005) Structural and functional studies of vertebrate metallothioneins: cross-talk between domains in the absense of physical contact. *Biochem. J. 391*, 95–103.

31. Ngu, T., Easton, A., and Stillman, M. J. (2008) Kinetic analysis of arsenic metalation of human metallothionein: significance of the two-domain structure. *J. Am. Chem. Soc. 130*, 17016–17028.
32. Xiong, Y., Zhou, Y., Chen, Y., and Ru, B. (1999) in Metallothionein IV (Klaassen, C. D., Ed.) pp 145−153, Birkhauser Verlag, Boston, MA.
33. Zangger, K., and Armitage, I. M. (2002) Dynamics of interdomain and intermolecular interactions in mammalian metallothioneins. *J. Inorg. Biochem. 88*, 135–143.
34. Zhou, Y., Li, L., and Ru, B. (2000) Expression, purification and characterization of $\beta$ domain and $\beta$ domain dimer of metallothionein. *Biochim. Biophys. Acta 1524*, 87–93.
35. Daneshfar, R., Kitova, E. N., and Klassen, J. S. (2004) Determination of protein-ligand association thermochemistry using variable-temperature nanoelectrospray mass spectrometry. *J. Am. Chem. Soc. 126*, 4786–4784.
36. Yu, X., Wojciechowski, M., and Fenselau, C. (1993) Assessment of metals in reconstituted metallothioneins by electrospray mass spectromentry. *Anal. Chem. 65*, 1355–1359.
37. Zaia, J., Fabris, D., Wei, D., Karpel, R. L., and Fenselau, C. (1998) Monitoring metal ion flux in reactions of metallothionein and drug-modified metallothionein by electrospray mass spectrometry. *Protein Sci. 7*, 2398–2404.
38. Shoemaker, G. K., Kitova, E. N., Palcic, M. M., and Klassen, J. S. (2007) Equivalency of binding sites in protein-ligand complexes revealed by time-resolved tandem mass spectrometry. *J. Am. Chem. Soc. 129*, 8674–8675.
39. Wilson, D. J., and Konermann, L. (2004) Mechanistic studies on enzymatic reactions by electrospray ionization MS using a capillary mixer with adjustable reaction chamber volume for time-resolved measurements. *Anal. Chem. 76*, 2537–2543.
40. Zechel, D. L., Konermann, L., Withers, S. G., and Douglas, D. J. (1998) Pre-steady state kinetic analysis of an enzymatic reaction monitored by time-resolved electrospray ionization mass spectrometry. *Biochemistry 37*, 7664–7669.
41. Sturzenbaum, S. R., Winters, C., Galay, M., Morgan, A. J., and Kille, P. (2001) Metal ion trafficking in earthworms: identification of a cadmium-specific metallothionein. *J. Biol. Chem. 276*, 34013–34018.
42. Sturzenbaum, S. R., Kille, P., and Morgan, A. J. (1998) The identification, cloning and characterization of earthworm metallothionein. *FEBS Lett. 431*, 437–442.
43. Chan, J., Huang, Z., Watt, I., Kille, P., and Stillman, M. J. (2007) Characterization of the conformational changes in recombinant human metallothioneins using ESI-MS and molecular modeling. *Can. J. Chem. 85*, 898–912.
44. Rey, N. A., Howarth, O. W., and Pereira-Maia, E. C. (2004) Equilibrium characterization of the As(III)-cysteine and the As(III)-glutathione systems in aqueous solution. *J. Inorg. Biochem. 98*, 1151–1159.
45. Serves, S. V., Charalambidis, Y. C., Sotiropoulos, D. N., and Ioannou, P. V. (1995) Reactions of arsenic(III) oxide, arsenous and arsenic acids with thiols. *Phoshorus, Sulfur Silicon Relat. Elem. 105*, 109–116.
46. Klein, D., Lichtmannegger, J., Heinzmann, U., Muller-Hocker, J., Michaelsen, S., and Summer, K. H. (1998) Association of copper to metallothionein in hepatic lysosomes of Long-Evans cinnamon (LEC) rats during the development of hepatitis. *Eur. J. Clin. Invest. 28*, 302–310.
47. Freedman, J. H., Powers, L., and Peisach, J. (1986) Structure of the copper cluster in canine hepatic metallothionein using X-ray absorption spectroscopy. *Biochemistry 25*, 2342–2349.
48. Morgan, A. J., Sturzenbaum, S. R., Winters, C., Grime, G. W., Aziz, N. A. A., and Kille, P. (2004) Differiential metallothionein expression in earthworm (*Lumbricus rubellus*) tissues. *Ecotoxicol. Environ. Saf. 57*, 11–19.
49. Attwood, P. V., and Geeves, M. A. (2004) Kinetics of an enzyme-catalyzed reaction measured by electrospray ionization mass spectrometry using a simple rapid mixing attachment. *Anal. Biochem. 334*, 382–389.
50. Ngu, T., Sturzenbaum, S. R., and Stillman, M. J. (2006) Cadmium binding studies to the earthworm *Lumbricus rubellus* metallothionein by electrospray mass spectrometry and circular dichroism spectroscopy. *Biochem. Biophys. Res. Commun. 351*, 229–233.
51. Housecroft, C. E., and Sharpe, A. G. (2005) Inorg. Chem. , 2nd ed., Pearson Prentice Hall, Harlow, England.
52. Shi, W., Dong, J., Scott, R. A., Ksenzenko, M. Y., and Rosen, B. P. (1996) The role of arsenic-thiol interactions in metalloregulation of *ars* operon. *J. Biol. Chem. 271*, 9291–9297.
53. Kagi, J. H. R., and Kojima, Y. (1985) Metallothionein II , Vol. 2, 1st ed., Birkhauser, Boston, MA.
54. Kagi, J. H. R., and Nordberg, M. (1978) Metallothionein , Vol. 1, 1st ed., Birkhauser, Boston, MA.